Total projectile electron loss cross sections of U^{28+} ions in collisions with gaseous targets ranging from hydrogen to krypton

G. Weber,[1,2,*] M. O. Herdrich,[1,3] R. D. DuBois,[4] P.-M. Hillenbrand,[2] H. Beyer,[2] L. Bozyk,[2]
T. Gassner,[1,3] R. E. Grisenti,[2,5] S. Hagmann,[2] Yu. A. Litvinov,[2] F. Nolden,[2] N. Petridis,[2,5,6]
M. S. Sanjari,[6] D. F. A. Winters,[2] and Th. Stöhlker[1,2,3]

[1]*Helmholtz-Institut Jena, 07743 Jena, Germany*
[2]*GSI Helmholtzzentrum für Schwerionenforschung, 64291 Darmstadt, Germany*
[3]*Institut für Optik und Quantenelektronik, Friedrich-Schiller-Universität, 07743 Jena, Germany*
[4]*Missouri University of Science and Technology, Rolla, Missouri 65409, USA*
[5]*Institut für Kernphysik, Johann Wolfgang Goethe-Universität, 60438 Frankfurt, Germany*
[6]*Extreme Matter Institute EMMI and Research Division, GSI Helmholtzzentrum für Schwerionenforschung,
64291 Darmstadt, Germany*

Beam lifetimes of stored U^{28+} ions with kinetic energies of 30 and 50 MeV/u, respectively, were measured in the experimental storage ring of the GSI accelerator facility. By using the internal gas target station of the experimental storage ring, it was possible to obtain total projectile electron loss cross sections for collisions with several gaseous targets ranging from hydrogen to krypton from the beam lifetime data. The resulting experimental cross sections are compared to predictions by two theoretical approaches, namely the CTMC method and a combination of the DEPOSIT code and the RICODE program.

I. INTRODUCTION

Charge-changing processes, i.e., loss or capture of electrons, occurring in ion-atom and ion-ion collisions belong to the most basic interactions in all types of plasmas and also in accelerator facilities. Besides basic research, the investigation of these processes is also motivated by their paramount importance for many applications, such as ion stripping and beam transport in accelerators and storage rings [1–3] as well as ion-driven fusion devices [4–6]. Essential here is that interactions between projectile ions and constituents of the residual gas can lead to a change of the projectile charge state. In the presence of dispersive ion optical elements the trajectories of these up- or down-charged ions are not matching the one of the reference charge state, resulting in a successive defocusing or even loss of the ion beam. Moreover, projectiles impinging on the walls of the beam lines give rise to several unwanted effects, such as increased radiation levels, damaging of sensitive instruments, and significant degrading of the vacuum conditions due to ion-impact induced desorption. For fast heavy ions the latter can lead to the release of up to 10^5 particles per incident ion, see [7,8] and references therein. At high beam intensities and repetition rates, this so-called dynamic-vacuum effect can even end up in an

avalanche process resulting in an almost instantaneous loss of the complete beam. Therefore, exact knowledge of the charge-changing cross sections is of crucial importance for the planning of ion-beam experiments in existing accelerators and storage rings as well as for the design of new facilities or upgrade programs.

This is particularly evident for the new facility for antiproton and ion research (FAIR), currently under construction near the center for heavy ion research GSI, where future ion-beam experiments will require unprecedented luminosities [9]. In order to reach the necessary beam intensities, while minimizing the limitations induced by space charge, and avoiding losses in stripper targets, the use of low to medium-charged, many-electron ions, namely U^{28+}, is planned. The existing heavy-ion synchrotron SIS18 of the GSI facility will serve as an injector for the new SIS100, which will be the main workhorse of the new facility providing U^{28+} beams with 5×10^{11} ions and energies up to 2.7 GeV/u [10]. To meet this specifications, the SIS18 will have to deliver more than 1×10^{11} U^{28+} ions with an energy of 200 MeV/u and a repetition rate of 2.7 Hz. However, in 2007 dynamical vacuum effects as described above limited the maximum number of extracted particles for this ion species to 6.5×10^9 [11]. Since then, major efforts were undertaken in order to reduce the vacuum base pressure and to minimize ion-induced desorption throughout the SIS18 beam line, leading recently to a new extraction record of 3.2×10^{10} accelerated U^{28+} ions [12,13].

In the energy region from roughly 10 MeV/u up to a few GeV/u the number of bound electrons of low-charged, many-electron ions, such as U^{28+}, is far above that of the

---

*g.weber@gsi.de

corresponding equilibrium charge state [14,15]. As a consequence, projectile ionization, sometimes also referred to as stripping or electron loss (EL), is the dominant beam loss process. While the theoretical description of ionization of few-electron ions, such as H-like and He-like systems, leads to reliable results within an uncertainty of 20% to 30% for a large range of collision energies and atomic numbers Z [16–18], calculations involving many-electron projectiles are still a challenging task [2,19]. To benchmark the theoretical approaches and semiempirical scaling laws developed for such systems, experimental data covering a wide range of collision energies as well as ion species and target systems are needed. Previous experimental studies of the EL cross sections of low-charged, heavy ions were mainly restricted to energies below 10 MeV/u [20–30], whereas for ion-driven fusion scenarios beam energies ranging from about 15 MeV/u up to roughly 500 MeV/u [31] are most relevant and in case of the FAIR facility the energy region of interest even extends up to the relativistic GeV/u regime.

Recently, we presented a first EL cross section measurement for a low-charged ion, namely U^{28+}, covering beam energies up to 50 MeV/u that was performed at the experimental storage ring (ESR) of the GSI Helmholtz Center for Heavy Ion Research [32]. In the present work, we report on a follow-up experiment using again U^{28+} projectiles which was performed under improved experimental conditions and with target gases covering a broader range of the atomic number Z. The experimental data are compared to predictions based on a combination of a classical deposition model (DEPOSIT code) [33,34] and the relativistic ionization code (RICODE) developed by Shevelko *et al.* [35] and, where available, to *n*-body classical trajectory Monte Carlo (CTMC) calculations by Olson [29].

II. MEASUREMENT TECHNIQUE AND DATA ANALYSIS

At GSI, U^{28+} ions were pre-accelerated in the Universal Linear Accelerator (UNILAC) and subsequently injected into the heavy ion synchrotron SIS18 where the projectiles were further accelerated to beam energies of 30 and 50 MeV/u, respectively. To perform cross section measurements, the ions were then injected into the ESR storage ring where they were stored with typical beam intensities of a few times 10^7 particles (equals to beam currents in the order of 0.1 mA). Note that while the SIS18 has a magnetic rigidity of 18 Tm allowing acceleration and storage of U^{28+} beams with energies up to approximately 200 MeV/u, the limitation to 10 Tm in the ESR leads to a maximum energy of approximately 60 MeV/u for this ion species. After injection into the ESR a high beam quality was achieved using the electron cooler, resulting in a strongly reduced emittance and a typical beam diameter in the order of 2 mm as well as a momentum spread in the order of

$\Delta p/p = 10^{-5}$ [36]. After a cooling time of a few seconds when stable beam conditions were reached, the shutter of the internal gas target was opened and a gas jet having a diameter in the order of $\Delta x = 5$ mm and being perpendicular to the ion beam axis was formed inside the interaction chamber of the ESR. Up- or down-charged ions produced in interactions with the target gas were subsequently lost due to collisions with the beam line walls or dedicated scrapers after passing the bending magnets. Moreover, the target density was chosen in such a way that charge-changing reactions between the gas jet and the ion beam were the dominant beam-loss processes compared to interactions with the residual gas and recombination in the electron cooler. After the beam intensity had fallen below the detection threshold, a new injection from the SIS18 was requested and the next measurement cycle was started.

Besides molecular hydrogen (H_2) and nitrogen (N_2), often used as reference components to model typical residual gas compositions in ultra-high vacuum environments, also neon, argon, and krypton were used as target gases with densities between a few times 10^9 and a few times 10^{11} particles/cm^3. These target densities resulted in a significant reduction of ion beam lifetimes to typical values of about a few seconds (compared to roughly 20 s without the gas target). The best target-beam overlap was found by scanning the ion beam axially across the target region in the interaction chamber while monitoring variations of the beam lifetime as well as the count rates of a photomultiplier and an electron spectrometer [37,38] observing the interaction region. More specifically, the beam lifetime was deduced from measuring the ion beam intensity as a function of time using a DC current transformer and the integrated Schottky signal of the new resonant pickup at the ESR [39]. Note that both instruments are complementary to each other as the current transformer is limited to ion currents above a few times 10^{-3} mA, whereas the Schottky diagnosis can detect very low beam intensities down to a few ions while at the same time exhibiting nonlinearities at beam currents above 0.01 mA (equals to 2.55×10^6 U^{28+} ions at a beam energy of 50 MeV/u) [40]. The ability to follow the decay of the ion beam intensity over several orders of magnitude using the Schottky signal and the electron spectrometer rate was a significant improvement compared to our previous study at the gas target where only the current transformer signal and a photomultiplier were available [32].

Once maximum overlap was established, the beam lifetime was measured several times for each beam energy and target species. A typical measurement cycle is shown in Fig. 1 where the signals of the beam transformer and the Schottky diagnostic are plotted as a function of time together with the count rate of an electron spectrometer located downstream of the interaction chamber as well as the density of the gas jet. The electron spectrometer was set to record free electrons moving at the same speed as the
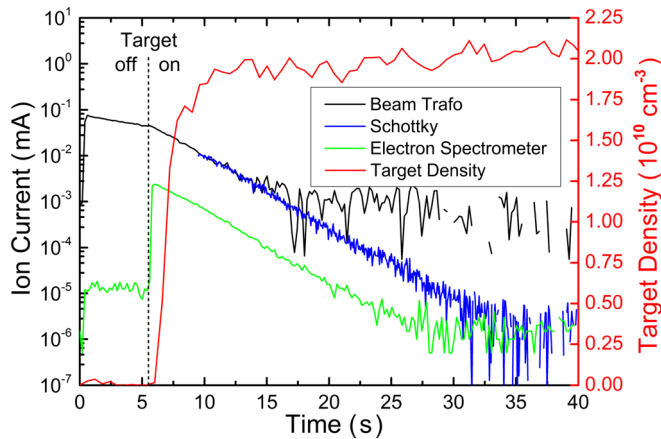
FIG. 1.   Beam intensity measured by a beam transformer and the Schottky diagnosis for a typical measurement cycle (50 MeV/u $U^{28+} \rightarrow$ Ar) plotted together with the rate of the electron spectrometer (in arbitrary units) and the target density (right ordinate). After the target is switched on a strong decrease of the beam lifetime is visible. The delayed rise of the gas target density is a measurement artefact (see text for details). In contrast to the current transformer, where a minimum background level is reached, the Schottky signal and the electron spectrometer rate allow following the decay of the ion beam intensity over several orders of magnitude. This is a major improvement compared to previous beam lifetime measurements.

projectile ions. Such electrons are mainly produced by projectile ionization within the beam-target overlap region and consequently the signal is in a good approximation proportional to the product of ion beam intensity and the gas target density, i.e., the luminosity.

As can be seen, the beam intensity $I(t)$ follows an exponential decay law,

$$I(t) = I(0) \exp(-\lambda t), \tag{1}$$

with t denoting the time and λ the decay constant. The latter is related to the beam lifetime τ by $\lambda = 1/\tau$. Therefore, λ, and consequently τ, can be obtained by adjusting Eq. (1) to the slope of the measured beam intensity as a function of time. In our analysis we used a mean λ by averaging the decay constants of the beam transformer, the Schottky signal and the electron spectrometer rate. In general, the beam lifetimes in the ESR are determined by

$$\tau^{-1} = \rho_{gt}\sigma_{gt}vf + \rho_{rg}\sigma_{rg}v + \lambda_{ec}, \tag{2}$$

where ρ_{gt} and ρ_{rg} are the densities of the gas target and the residual gas throughout the ring, respectively, while σ_{gt} denotes the charge-changing cross section for the target gas and σ_{rg} is the weighted mean of the individual cross sections for the different residual gas components. Note that we assume the residual gas pressure and composition to remain constant during the measurement, i.e., the absence of dynamical vacuum effects. This assumption is justified for low beam intensities combined with not too

high loss rates, as was the case in the present experiment. The recombination rate in the electron cooler is taken into account by λ_{ec}. Finally, the projectile velocity is given by v and f is the fractional length of the interaction region compared to the full cycle length (108.4 m for the ESR), e.g., $f = 1$ in the case of interactions with the residual gas covering the whole ring. In order to extract the lifetime due to interactions with the gas target only, the contribution of the residual gas $\rho_{rg}\sigma_{rg}v$ and the electron cooler λ_{ec} to the total beam loss rate were subtracted. The sum of both quantities was obtained for each measurement cycle during the time between injection of the ion beam into the ESR and the start of the target (cf. Fig. 1) as well as in dedicated measurements during which the target shutter was closed for the whole cycle. In this measurements without a gasjet being present beam lifetimes of about 20 s were obtained which roughly corresponds to an average base pressure in the order of a few times 10^{-11} mbar throughout the storage ring. Monitoring the stability of this "background lifetime" also ensured that we did not significantly deteriorate the ESR vacuum conditions by the operation of the gas target.

For analyzing the ion beam lifetime due to charge exchange in interaction with the target, the fractional target length in Eq. (2) needs to be known. In previous studies, a value of $f = 0.005/108.4$ for the interaction length between the ion beam and the target was used. This value, which corresponds to a diameter of the gas jet of 5 mm at the intersection point with the ion beam, was determined by the skimmer geometry of the target apparatus and was also verified experimentally, see [41,42]. However, recent investigations indicate that the upgrade of the target apparatus a few years ago [43] gave rise to a slight modification of the target profile. More specific, a recent spatial characterization of the target shape, that was performed by members of the FOCAL collaboration [44], yielded a flat-top target profile with a mean diameter of $\Delta x = 6.4$ mm and slightly fuzzy edges [45,46] at the interaction point with the ion beam. In this study a thin wire that was blocking a small portion of the gas jet was moved through the target and the partial-pressure increase corresponding target gas type was analyzed in the interaction chamber. The resulting model for the radial gas jet profile is given by [46]

$$\rho(r) = \frac{1}{2}\mathrm{erf}\left(\frac{\frac{\Delta x}{2} - r}{\sqrt{2}\sigma}\right) + \frac{1}{2}, \tag{3}$$

where the parameter σ, that has an approximate value of 0.3 mm, determines the "fuzziness" of the edges of the target density profile. To verify this new target model, we numerically convoluted the target profile with a Gaussian shaped ion beam with a realistic $\sigma = 1.5$ mm and compared the result to a recent measurement series [47], where the ion beam axis was moved horizontally through the target jet and the charge exchange rate, i.e., the effective overlap between ion beam and target, was recorded. This

comparison is presented in Fig. 2, where it is clearly seen that the model from Eq. (3) yields a significantly better agreement than old model of a 5 mm thick target. Consequently, we used a new "effective" target length of $f = 0.0059/108.4$, yielded by the superposition of the Gaussian shaped ion beam with the new target profile under assumption that the ion beam hits in the target center.

The average gas target density ρ_{gt} was obtained from the pressure increase p_i measured by ionization vacuum gauges in the four dump stages of the gas target using the following equation:

$$\rho_{gt} = \frac{4}{\pi \Delta x^2} \frac{1}{k_B T v_{gas}} \sum_{i=1}^{4} S_i p_i, \qquad (4)$$
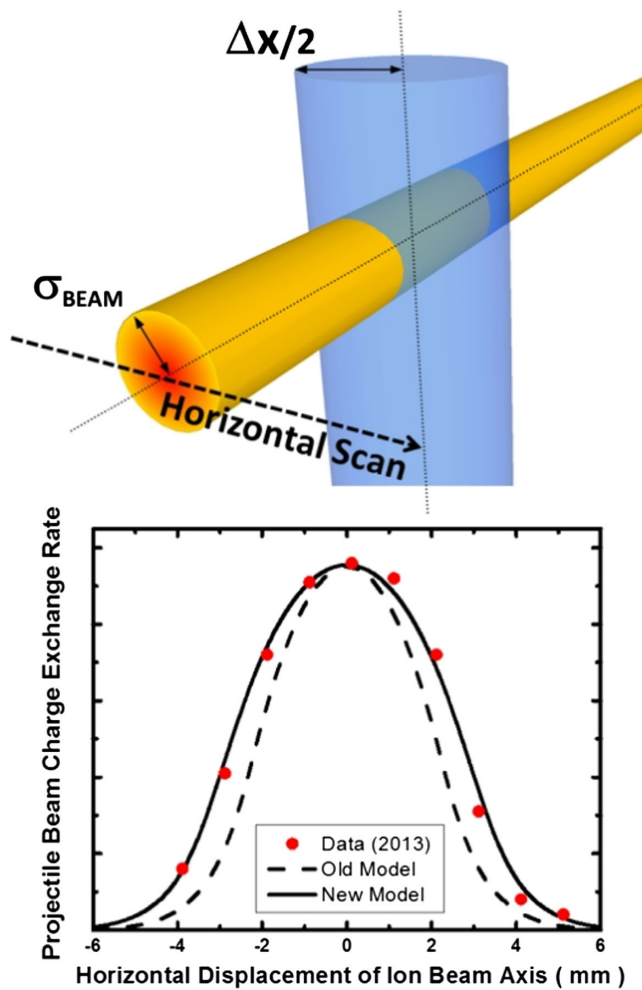

FIG. 2. Verification of the assumed spatial profile of the target jet: The new and the previous target models were convoluted numerically with a Gaussian shaped ion beam in order to reproduce experimental data for the effective overlap between target and ion beam [47]. The latter is given by the projectile charge exchange rate that was measured as a function of the horizontal position of the ion beam axis. The new model yields good agreement with experiment. See text for details.

where Δx is the gas jet diameter [the slight fuzziness of the edges from Eq. (3) can be safely ignored here], k_B denotes the Boltzmann constant and S_i is the gas-dependent suction capacity (according to manufacturer specifications) of the TMPs installed at the four differential pumping stages of the target dump. Along its passage through the interaction chamber only a minor fraction of the particles within the gas jet is evaporated or kicked out in hard collisions with the projectile beam, resulting in a nearly 100% collection efficiency of the gas load within the dump section of the target installation. For a detailed description of the internal gas target at the ESR the reader is referred to [41–43]. However, one has to note that in Eq. (4) an equilibrium between gas load and TMP pumping power is assumed which is not immediately the case after opening the target valve. Moreover, the ionization gauges are averaging the measured gas pressure over a time period of about 1 s. Consequently, in our analysis the target density was obtained only for the quasiconstant region that establishes a few seconds after the target is switched on (cf. Fig. 1). Finally, the T in Eq. (4) denotes the gas temperature when being pumped away by the turbo molecular pumping (TMP) system after hitting the chamber wall in the last dump stage, i.e., roughly 300 K, and v_{gas} is the gas speed after the expansion through the nozzle. The latter quantity depends on the inlet pressure p_0 (typically about 10 bar) and the nozzle temperature T_0 (ranging from about 40 K for H_2 up to room temperature for the high-Z nobel gases). More specifically, the gas speed is determined by the conversion process of internal energy into directed kinetic energy, which takes place during the expansion of the gas through a nozzle into vacuum. For the present work, two different approaches were used for the calculation of the gas speed depending on the nozzle conditions. For $T_0 \gg T_{crit}$, where T_{crit} is the critical temperature of the applied target gas, the process is regarded as an ideal gas expansion. Consequently, a total conversion into directed kinetic energy is assumed thus a simplified formula for the velocity calculation is deduced [48]:

$$v_{gas} = v_{ideal} = \sqrt{\left(\frac{2\kappa}{\kappa - 1}\right) \frac{k_B}{m} T_0}. \qquad (5)$$

Here, $\kappa(T, p) = c_p/c_V$ is the adiabatic index of the applied target gas, with $c_{p,V}$ being the heat capacity at constant pressure and volume, respectively, and m is the particle mass. This equation is applicable for an expansion of a gaseous fluid where no significant clusterization (condensation) processes take place.

In case of an expansion from the fluids supercritical phase ($p_0 > p_{crit}$, $T_0 \rightarrow T_{crit}$) the ideal gas approximation becomes invalid. Hence, the gas speed is calculated by a more general approach that solely takes the initial enthalpy h_0 (before the expansion) and the final enthalpy h (after the expansion process took place) into account. The corresponding equation is given by

$$v_{\text{gas}} = v_{\text{crit}} = \sqrt{\frac{2}{m}(h_0 - h)}. \qquad (6)$$

The initial enthalpy for given nozzle conditions is readily provided by the NIST database [49] whereas the final enthalpy of the target beam cannot be determined precisely. An approximation proposed by Christen *et al.* [50] was therefore used, which assumes that the isentropic expansion process of the target beam ceases at the triple point. Thus, the triple point enthalpy h_{tp} of the target gas is used as the final enthalpy value. Since condensation processes take place during an isentropic expansion at these conditions, both the liquid enthalpy $h_{\text{tp,l}}$ as well as the vapor enthalpy $h_{\text{tp,v}}$ have to be considered. A reasonable fit of the calculation with experimental data (taken from Knuth *et al.* [51]) was found by assuming $h = 0.5h_{\text{tp,l}} + 0.5h_{\text{tp,v}}$ for the final enthalpy [52]. A reliable value for the gas velocity can thus be calculated according to the expansion conditions of the fluid.

As already mentioned above, at the beam energies under investigation projectile EL is by far the dominant beam loss process for low-charged, many-electron ions, while the contribution of capture of target electrons can safely be neglected. Therefore, we assume that all beam losses caused by the gas target can be attributed to projectile electron-loss. As a consequence, projectile EL cross sections for each target gas can be obtained by solving Eqs. (1) and (2) combined with the gas target density yielded by Eq. (4). Moreover, as a charge-state resolved detection of up- or down-charged ions was not possible, the following discussion is restricted to the total EL cross section.

III. RESULTS AND DISCUSSION

In Fig. 3 the total EL cross sections per target atom for U^{28+} obtained in this work as well as previous experimental results (taken from [20,21,29,30,32]) are compared to theoretical predictions by the CTMC method of Olson *et al.* [29] and recent results based on a combination of the DEPOSIT code and the RICODE (DEPOSIT + RICODE) provided by V. P. Shevelko *et al.* [53]. Unfortunately, CTMC results for U^{28+} electron loss are only published for H, N, and Ar as targets. Note that we assume that for H_2 and N_2 the influence of the molecular binding on the ionization process is negligible and, consequently, the molecular cross section is given as the sum of individual target atoms as was previously shown for Xe^{18+} at a collision energy of 6 MeV/u [27]. The error bars of the present data points result from a statistical analysis of the cycle-to-cycle variations of the obtained cross section data combined with the uncertainty of the gas velocity (between 0% and 15%) and a 20% systematic uncertainty in the estimation of the gas pressure in the target dump. The latter accounts for the uncertainty in the gas-dependent correction factors of both the ionization gauges and the TMP pumping powers at the dump section of the target apparatus. For the
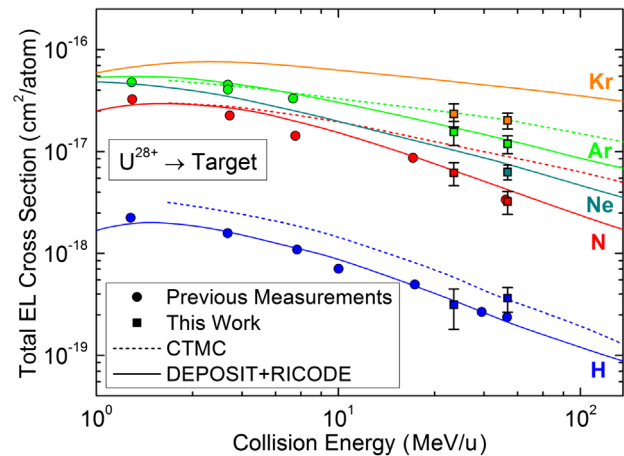

FIG. 3.   Experimental total electron loss cross sections of U^{28+} ions in comparison to calculations performed by Shevelko *et al.* (DEPOSIT + RICODE) [53] and by Olson *et al.* (CTMC) [29]. Values for H and N were obtained by dividing the measurements for the molecular targets by a factor of 2. While both theories are in qualitative agreement with the experimental data for H, the CTMC results significantly overestimate the cross section for N and Ar. In contrast, DEPOSIT + RICODE predictions are in good agreement with experimental results for all targets but for the heaviest one, namely Kr.

H_2 target, the unphysical energy-dependence obtained in this measurement is most probably due to instabilities of the nozzle temperature which are also reflected by a larger experimental uncertainty compared to the other targets that were operated at much higher nozzle temperatures. All experimental data available for total electron-loss cross sections of U^{28+} projectiles are also presented in Table I.

As can be seen in Fig. 3, the experimental values for total electron loss of U^{28+} in collisions with hydrogen and nitrogen obtained in this work show good qualitative agreement with the previous measurement at the ESR gas target [32]. Moreover, the cross sections yielded by both theoretical approaches and the experimental data for the hydrogen target all exhibit a very similar energy dependence in the energy regime above a few MeV/u, while the absolute values of the two models differ approximately by a factor of 1.5. Even though most experimental values lie closer to the calculations by Shevelko *et al.*, when taking into account the limited accuracy of the theoretical approaches, both calculations as well as the experimental results are in agreement with each other. This finding for the H_2 target is contrasted by a clear deviation of the experimental values for all heavier targets toward lower cross section values when compared to CTMC predictions. While the data from Shevelko *et al.* agree with the measured cross sections within a factor of roughly 1.5 for all targets except for krypton, the deviation from the CTMC data is significantly larger (up to a factor 2.5). Already in our previous measurements a large discrepancy between CTMC predictions and experimental data was

TABLE I. Experimental cross sections for total electron loss of U^{28+} ions in collisions with gaseous targets. Previous data are taken from Franzke [21], Erb [20], Olson *et al.* [29], Perumal *et al.* [30], and Weber *et al.* [32]. In case of the Franzke data the values result from an interpolation between measurements for U^{20+} and U^{30+} ions, while the Erb value was obtained by a similar interpolation between data points for U^{27+} and U^{30+}. Uncertainties are given if available.

Collision Energy (MeV/u)	Target Gas	Total EL Cross Section (10^6 barn/atom)
1.4	H_2	2.25 [21]
	N_2	32.60 [21]
	Ar	47.80 ± 6.70 [20]
3.5	H_2	1.62 ± 0.35 [29]
	N_2	22.52 ± 1.07 [29]
	Ar	45.38 ± 1.62 [29]
		40.65 ± 1.65 [30]
6.5	H_2	1.14 ± 0.26 [29]
	N_2	14.69 ± 0.82 [29]
	Ar	33.15 ± 1.25 [29]
10	H_2	0.74 ± 0.18 [32]
20	H_2	0.51 ± 0.13 [32]
	N_2	8.80 ± 2.20 [32]
30	H_2	0.31 ± 0.13
	N_2	6.21 ± 1.56
	Ar	15.61 ± 4.09
	Kr	23.37 ± 5.96
40	H_2	0.28 ± 0.07 [32]
50	H_2	0.25 ± 0.06 [32] 0.36 ± 1.00
	N_2	3.48 ± 0.87 [32] 3.24 ± 0.82
	Ne	6.33 ± 1.04
	Ar	11.93 ± 2.40
	Kr	20.22 ± 3.61

found for N_2 as a target, whereas the agreement with the data by Shevelko *et al.* (using the LOSS-R code [54], the predecessor of the RICODE) was better. While at that time only two data points above 10 MeV/u with severe experimental uncertainties were available, the present data set affirms this finding for nitrogen and also argon.

The deviation between the two theoretical models results from their different scaling of total EL as a function of the projectile energy E in the region above 10 MeV/u. For the H_2 target where the ionization process is expected to be dominated by single electron loss, both models exhibit an E^{-1} scaling which is typical for single electron, first-order perturbative approaches. In contrast, for the N_2 and the Ar targets the cross sections yielded by DEPOSIT + RICODE scale with $E^{-0.8}$ and $E^{-0.5}$, respectively, whereas the corresponding values for the CTMC results are $E^{-0.5}$ and $E^{-0.3}$. These differences can most probably be attributed to the influence of multiple-electron loss processes as it is known that for many-electron ions colliding with heavy targets the contribution of ionization events, where more than one projectile electron is removed, can amount to 50% or more [2,27]. In the treatment by Shevelko *et al.*, the

RICODE is restricted to single electron ionization showing an E^{-1} scaling independent of the target system. Only by the combination with the DEPOSIT code multielectron processes are taken into account in a rather approximate way (see [34,35] for details). In contrast, *n*-body CTMC calculations are capable to incorporate explicitly all involved particles allowing a rigorous treatment of multi-electron processes. Thus, for many-electron projectiles, such as U^{28+}, colliding with many-electron targets like N_2 and Ar, where multielectron processes are likely to form a major component of the total cross section, one would expect the CTMC method to agree with experiment better than a single-electron model such as the RICODE method. Therefore, as already pointed out in our previous study [32], the large discrepancy between CTMC predictions and the present experimental data that is found in particular for the heavy target systems is surprising. However, it was shown by Kaganovich and co-workers that reliable projectile electron-loss cross sections even for high-Z targets can be obtained when a hybrid approach is used, in which only "hard" collisions at small impact parameters are treated using CTMC methods while for distant collisions a quantum-mechanical perturbative description is applied [55]. Such an approach, which allows switching between various treatments according to the different collision parameter ranges in which each of them can be expected to have the greatest validity, might prove to be of particular value when complex collision systems are studied.

This is even more so since also the DEPOSIT + RICODE results, despite being in much better agreement with measurements compared to the CTMC data, show a significant deviation towards higher cross section for the heaviest target, namely krypton. This feature is illustrated in Fig. 4, where the dependence on the target atomic number Z is presented for the U^{28+} electron loss cross sections at beam energies of 30 and 50 MeV/u, respectively. Note that at 50 MeV/u the corresponding two data points available for H_2 and N_2 targets were averaged. The experimental data are compared to both, DEPOSIT + RICODE and CTMC results, as well as to the $Z^2 + Z$ target scaling obtained from first-order perturbation theory (Born scaling). In general, a deviation of the projectile EL cross section from the Born scaling can be attributed to shielding, sometimes also referred to as screening, of the target nuclear charge by the target electrons and to the fact that inner-shell target electrons can be regarded as "inactive" with respect to projectile EL at large impact parameters due to their stronger localization. In addition, for many-electron projectiles colliding with heavy targets the probability of ejection of at least one electron, i.e., the total electron loss, can approach 1 for a significant range of the impact parameter. In this situation a further increase of target Z only leads to a higher average number of lost electrons, whereas the total electron-loss cross section remains nearly constant. The present data indicate that
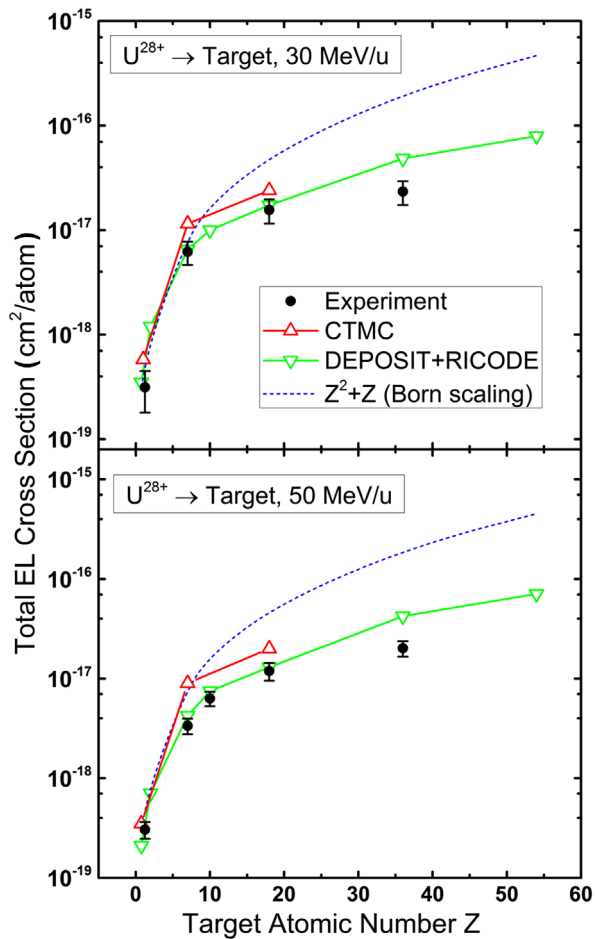
FIG. 4. Target Z dependence of the measured total electron loss cross sections in comparison to calculations performed by Shevelko *et al.* (DEPOSIT + RICODE) [53] and by Olson *et al.* (CTMC) [29] as well as to the $Z^2 + Z$ scaling obtained from first-order perturbation theory ("Born scaling"). Solid lines between the theory data points are drawn to guide the eye. Moreover, the experimental and theory data points for the hydrogen target were slightly shifted against each other along the abscissa.

both theoretical models are not able to fully reproduce these effects on the total projectile EL by high-Z targets. However, for the targets most relevant for residual gas modeling, namely H_2, N_2 and Ar, the DEPOSIT + RICODE treatment yields a reasonable approximation. Moreover, the reader should note that very recently and improved version of the RICODE (now called RICODE-M) was presented [56] which uses more realistic electron wave functions for high-Z systems.

IV. SUMMARY AND CONCLUSIONS

Total projectile electron loss cross sections of U^{28+} ions in collisions with various gaseous targets ranging from molecular hydrogen to krypton were measured for beam energies of 30 and 50 MeV/u, respectively. The available experimental data were compared to two treatments for the collision of many-electron systems at moderate to high

collision energies, namely the CTMC method of Olson *et al.* and the DEPOSIT + RICODE approach developed by Shevelko and co-workers. While reasonable agreement is found between both theory models and experimental data for collisions with hydrogen targets, the DEPOSIT + RICODE results show a significantly better agreement with measurements for all the heavier targets. However, also these predictions from Shevelko *et al.* tend to significantly overestimate the electron loss cross sections for the heaviest target under investigation, namely krypton.

[1] Th. Stöhlker, T. Ludziejewski, H. Reich, F. Bosch, R. W. Dunford, J. Eichler, B. Franzke, C. Kozhuharov, G. Menzel, P. H. Mokler *et al.*, Phys. Rev. A **58,** 2043 (1998).

[2] V. P. Shevelko, M. S. Litsarev, Th. Stöhlker, H. Tawara, I. Y. Tolstikhina, and G. Weber, in *Atomic Processes in Basic and Applied Physics*, edited by V. Shevelko and H. Tawara (Springer Berlin, Heidelberg, 2012), p. 125.

[3] H. Imao, H. Okuno, H. Kuboki, S. Yokouchi, N. Fukunishi, O. Kamigaito, H. Hasebe, T. Watanabe, Y. Watanabe, M. Kase *et al.*, Phys. Rev. ST Accel. Beams **15,** 123501 (2012).

[4] T. Peter and J. Meyer-ter Vehn, Phys. Rev. A **43,** 2015 (1991).

[5] L. Grisham, Nucl. Instrum. Methods Phys. Res., Sect. A **464,** 315 (2001).

[6] R. Olson, Nucl. Instrum. Methods Phys. Res., Sect. A **464,** 93 (2001).

[7] C. Omet, P. Spiller, J. Stadlmann, and D. H. H. Hoffmann, New J. Phys. **8,** 284 (2006).

[8] E. Mahner, Phys. Rev. ST Accel. Beams **11,** 104801 (2008).

[9] FAIR Baseline Technical Report, 2006, available at: http://www.fair-center.eu/en/for-users/publications/fair-publications.html.

[10] P. Spiller and W. Barth, Nucl. Instrum. Methods Phys. Res., Sect. A **733,** 171 (2014).

[11] C. Omet and P. Spiller, in GSI Scientific Report 2007, GSI Library, 2008, p. 91, available at: http://repository.gsi.de/.

[12] L. Dahl, W. Barth, M. C. Bellachioma, L. Groening, O. Kester, M. Kirk, D. Ondreka, N. Pyka, P. Spiller, J. Stadlmann *et al.*, in *Proceedings of the 12th Heavy Ion Accelerator Technology Conference (HIAT2012), Chicago, Illinois USA* (2012), p. 211, available at: http://accelconf.web.cern.ch/Accelconf/HIAT2012/papers/thb04.pdf.

[13] Y. E. Hayek, U. Ratzinger, P. Spiller, D. Ondreka, and M. Kirk, in *Proceedings of the 4th International Particle*

Accelerator Conference, IPAC-2013, Shanghai, China, 2013 (JACoW, Shanghai, China, 2013), p. 300, available at: http://accelconf.web.cern.ch/accelconf/IPAC2013/papers/mopfi010.pdf.

[14] C. Scheidenberger, Th. Stöhlker, W. Meyerhof, P. Mokler, and B. Blank, Nucl. Instrum. Methods Phys. Res., Sect. B **142**, 441 (1998).

[15] G. Schiwietz and P. L. Grande, Nucl. Instrum. Methods Phys. Res., Sect. B **175–177**, 125 (2001).

[16] Th. Stöhlker, H. Geissel, H. Folger, C. Kozhuharov, P. Mokler, G. Münzenberg, D. Schardt, T. Schwab, M. Steiner, H. Stelzer et al., Nucl. Instrum. Methods Phys. Res., Sect. B **61**, 408 (1991).

[17] P. Rymuza, Th. Stöhlker, C. L. Cocke, H. Geissel, C. Kozhuharov, P. H. Mokler, R. Moshammer, F. Nickel, C. Scheidenberger, Z. Stachura et al., J. Phys. B **26**, L169 (1993).

[18] Th. Stöhlker, D. Ionescu, P. Rymuza, T. Ludziejewski, P. Mokler, C. Scheidenberger, F. Bosch, B. Franzke, H. Geissel, O. Klepper et al., Nucl. Instrum. Methods Phys. Res., Sect. B **124**, 160 (1997).

[19] I. D. Kaganovich, E. Startsev, and R. C. Davidson, New J. Phys. **8**, 278 (2006).

[20] W. Erb, Tech. Rep., GSI Report No. P-7-78, 1978, available at: https://www-alt.gsi.de/documents/DOC-2007-Oct-133-1.pdf.

[21] B. Franzke, IEEE Trans. Nucl. Sci. **28**, 2116 (1981).

[22] W. G. Graham, K. H. Berkner, R. V. Pyle, A. S. Schlachter, J. W. Stearns, and J. A. Tanis, Phys. Rev. A **30**, 722 (1984).

[23] D. Mueller, L. Grisham, I. D. Kaganovich, R. L. Watson, V. Horvat, K. E. Zaharakis, and M. S. Armel, Phys. Plasmas **8**, 1753 (2001).

[24] R. E. Olson, R. L. Watson, V. Horvat, and K. E. Zaharakis, J. Phys. B **35**, 1893 (2002).

[25] R. D. DuBois, A. C. F. Santos, R. E. Olson, Th. Stöhlker, F. Bosch, A. Bräuning-Demian, A. Gumberidze, S. Hagmann, C. Kozhuharov, R. Mann et al., Phys. Rev. A **68**, 042701 (2003).

[26] V. Horvat, R. Watson, K. Zaharakis, and Y. Peng, Nucl. Instrum. Methods Phys. Res., Sect. B **211**, 495 (2003).

[27] R. L. Watson, Y. Peng, V. Horvat, G. J. Kim, and R. E. Olson, Phys. Rev. A **67**, 022706 (2003).

[28] R. D. DuBois, A. C. F. Santos, Th. Stöhlker, F. Bosch, A. Bräuning-Demian, A. Gumberidze, S. Hagmann, C. Kozhuharov, R. Mann, A. Orsic-Muthig et al., Phys. Rev. A **70**, 032712 (2004).

[29] R. E. Olson, R. L. Watson, V. Horvat, A. N. Perumal, Y. Peng, and Th. Stöhlker, J. Phys. B **37**, 4539 (2004).

[30] A. Perumal, V. Horvat, R. Watson, Y. Peng, and K. Fruchey, Nucl. Instrum. Methods Phys. Res., Sect. B **227**, 251 (2005).

[31] P. A. Seidl, J. J. Barnard, A. Faltens, and A. Friedman, Phys. Rev. ST Accel. Beams **16**, 024701 (2013).

[32] G. Weber, C. Omet, R. D. DuBois, O. de Lucio, Th. Stöhlker, C. Brandau, A. Gumberidze, S. Hagmann, S. Hess, C. Kozhuharov et al., Phys. Rev. ST Accel. Beams **12**, 084201 (2009).

[33] V. P. Shevelko, M. S. Litsarev, and H. Tawara, J. Phys. B **41**, 115204 (2008).

[34] V. P. Shevelko, D. Kato, M. S. Litsarev, and H. Tawara, J. Phys. B **43**, 215202 (2010).

[35] V. P. Shevelko, I. L. Beigman, M. S. Litsarev, H. Tawara, I. Y. Tolstikhina, and G. Weber, Nucl. Instrum. Methods Phys. Res., Sect. B **269**, 1455 (2011).

[36] M. Steck, P. Beller, K. Beckert, B. Franzke, and F. Nolden, Nucl. Instrum. Methods Phys. Res., Sect. A **532**, 357 (2004).

[37] P.-M. Hillenbrand, S. Hagmann, D. Atanasov, D. Banas, K.-H. Blumenhagen, C. Brandau, W. Chen, E. De Filippo, A. Gumberidze, D. L. Guo et al., Phys. Rev. A **90**, 022707 (2014).

[38] P.-M. Hillenbrand, S. Hagmann, A. B. Voitkiv, B. Najjari, D. Banas, K.-H. Blumenhagen, C. Brandau, W. Chen, E. De Filippo, A. Gumberidze et al., Phys. Rev. A **90**, 042713 (2014).

[39] F. Nolden, P. Hülsmann, Y. Litvinov, P. Moritz, C. Peschke, P. Petri, M. Sanjari, M. Steck, H. Weick, J. Wu et al., Nucl. Instrum. Methods Phys. Res., Sect. A **659**, 69 (2011).

[40] M. S. Sanjari, P.-M. Hillenbrand, R. DuBois, F. Bosch, S. Hagmann, P. Hülsmann, C. Kozhuharov, Y. A. Litvinov, F. Nolden, C. Peschke et al., in GSI Scientific Report 2012, GSI Library, 2013, p. 359, available at: http://repository.gsi.de/.

[41] H. Reich, W. Bourgeois, B. Franzke, A. Kritzer, and V. Varentsov, Nucl. Phys. **A626**, 417 (1997).

[42] A. Krämer, A. Kritzer, H. Reich, and Th. Stöhlker, Nucl. Instrum. Methods Phys. Res., Sect. B **174**, 205 (2001).

[43] M. Kühnel, N. Petridis, D. F. A. Winters, U. Popp, R. Dörner, Th. Stöhlker, and R. E. Grisenti, Nucl. Instrum. Methods Phys. Res., Sect. A **602**, 311 (2009).

[44] S. Chatterjee, H. Beyer, D. Liesen, Th. Stöhlker, A. Gumberidze, C. Kozhuharov, D. Banas, D. Protic, K. Beckert, P. Beller et al., Nucl. Instrum. Methods Phys. Res., Sect. B **245**, 67 (2006).

[45] T. Gassner, in GSI Scientific Report 2013, GSI Library, 2014.

[46] T. Gassner and H. Beyer (to be published).

[47] N. Winters, Ph.D. thesis, University of Heidelberg, 2013.

[48] A. Gruber, W. Bourgeois, B. Franzke, A. Kritzer, and C. Treffert, Nucl. Instrum. Methods Phys. Res., Sect. A **282**, 87 (1989).

[49] NIST Chemistry Webbook, 2015, available at: http://webbook.nist.gov/chemistry/fluid.

[50] W. Christen, K. Rademann, and U. Even, J. Chem. Phys. **114**, 11189 (2010).

[51] E. L. Knuth, F. Schünemann, and J. P. Toennies, J. Chem. Phys. **102**, 6258 (1995).

[52] N. Petridis, Ph.D. thesis, University of Frankfurt, 2014.

[53] V. P. Shevelko, I. Y. Tolstikhina, and M. S. Litsarev (private communication).

[54] I. L. Beigman, I. Y. Tolstikhina, and V. P. Shevelko, Tech. Phys. **53**, 547 (2008).

[55] I. D. Kaganovich, E. A. Startsev, R. C. Davidson, in Proceedings of the 21st Particle Accelerator Conference, Knoxville, TN, 2005 (IEEE, Piscataway, NJ, 2005), p. 1988, available at: http://accelconf.web.cern.ch/AccelConf/p05/PAPERS/FPAP028.pdf.

[56] I. Y. Tolstikhina, I. I. Tupitsyn, S. N. Andreev, and V. P. Shevelko, J. Exp. Theor. Phys. **119**, 1 (2014).